Organic Electronics 53 (2018) 88–95

Contents lists available at ScienceDirect

Organic Electronics

journal homepage: www.elsevier.com/locate/orgel

Deciphering perovskite crystal growth in interdiffusion protocol for planar heterojunction photovoltaic devices

Jun Xi[a,c], Hua Dong[a], Chenxin Ran[a], Ting Lei[a], Bo Jiao[a], Xun Hou[a], Zhaoxin Wu[a,b,*]

[a] Key Laboratory of Photonics Technology for Information, Key Laboratory for Physical Electronics and Devices of the Ministry of Education, School of Electronic and Information Engineering, Xi'an Jiaotong University, Xi'an 710049, PR China
[b] Collaborative Innovation Center of Extreme Optics, Shanxi University, Taiyuan 030006, PR China
[c] Global Frontier Center for Multiscale Energy Systems, Seoul National University, Seoul 08826, South Korea

ARTICLE INFO

Keywords:
Interdiffusion protocol
Crystal growth
Nucleation *versus* coarsening
Perovskite films
Planar heterojunction

ABSTRACT

Hybrid organic-inorganic perovskites (HIOPs) have increasingly promoted the photovoltaic field due to their excellent semiconductor properties and inexpensive costs. Interdiffusion protocol has been regarded as an efficient approach to deposit high-quality HIOP films. Nevertheless, the underlying mechanism of this protocol remains obscured. In this work, in virtue of vapor-deposited lead halide frame to eliminate solution-driven lead halide effect, we thoroughly studied the evolution of different HIOP films by symmetrically controlling the initial lead halides as well as organic salts. The crystal growth mechanism of the interdiffusion can be drawn in two aspects: 1. CH_3NH_3 (MA)-HIOP shows higher nucleation rate than $(NH_2)_2CH$ (FA)-HIOP; 2. FA-HIOP and $PbCl_2$-HIOP exhibit greater coarsening rates than other colleagues. Most importantly, conflicting lattice with Cl-barren phase and Cl-rich phase is first uncovered for MA-HIOP and FA-HIOP using $PbCl_2$ frame. All the device performances based on these films also prove the potential mechanism, and champion efficiency of 16.01% is achieved based on $FAPbI_3$. This work will provide in-depth insight into the interdiffusion protocol and drive this protocol toward multiple photovoltaic applications by facilely controlling precursor compositions.

1. Introduction

Hybrid organic-inorganic perovskites (HIOPs), overwhelming other semiconductor materials, have tremendously boosted the photovoltaic field in recent years since Miyasaka et al. pioneered promising devices by simple solution method [1–3]. Moreover, the excellent photo-physical natures (such as tunable bandgap, high absorption coefficient, and long carrier diffusion length) make HIOPs increasingly intriguing [4–9]. The key for realizing highly efficient device lies in depositing high-quality polycrystalline HIOP films with lower roughness, higher film coverage, homogeneity and more favourable crystallinity. Multiple deposition protocols, proposed by many groups, have been applied for yielding high-quality films especially toward planar heterojunction (PHJ) architecture [10–20]. Among these approaches, interdiffusion of stacking layers, initially proposed by Xiao et al., became the most prevailing pathway to deposit uniform HIOP films [14]. Unfortunately, the individual roles of different halides in the initial lead halide (PbX_2) layer and different organic cations in the upper layer still remain unclear during interdiffusion process. First of all, various solubility of different PbX_2 compounds in particular solvent makes it difficult to deposit high-quality spin-coated matrix film to study halide-induced effect. Impressively, vapor deposition with higher accuracy is regarded as a beneficial method toward uniform lead halide films under low temperature irrespective of the PbX_2 [21–23]. Additionally, thanks to the easily processing various organic cations within HIOP structure [24–27], versatile bandgaps could be readily achieved by employing different PbX_2. However, the different ionic size between $CH_3NH_3^+$ (MA^+) as well as $(NH_2)_2CH^+$ (FA^+) will lead to distinct crystal growth kinetics, so as to the resulting films [2,28–30]. Consequently, the underlying growth mechanism of polycrystalline HIOP films driven by interdiffusion, based on varying PbX_2 matrixes and organic components, is an imperative issue to be addressed. Especially, when $PbCl_2$ is firstly served as the lead source, whether Cl^- inclusion in the final HIOP lattice or not is still under debate, indicating more complicated reacting mechanism compared to pure I^- phase during the conversion process [31–34].

In order to best comprehend the interdiffusion deposition for PHJ devices, we should analyze the independent role in nucleation as well as coarsening stages of the beneath PbX_2 layer and the upper organic salt (MAI/FAI) layer. In this work, we focus on the evolution process of the

* Corresponding author. Key Laboratory of Photonics Technology for Information, Key Laboratory for Physical Electronics and Devices of the Ministry of Education, School of Electronic and Information Engineering, Xi'an Jiaotong University, Xi'an 710049, PR China.
E-mail address: zhaoxinwu@mail.xjtu.edu.cn (Z. Wu).

https://doi.org/10.1016/j.orgel.2017.11.011
Received 5 September 2017; Received in revised form 7 November 2017; Accepted 8 November 2017
Available online 11 November 2017
1566-1199/ © 2017 Published by Elsevier B.V.

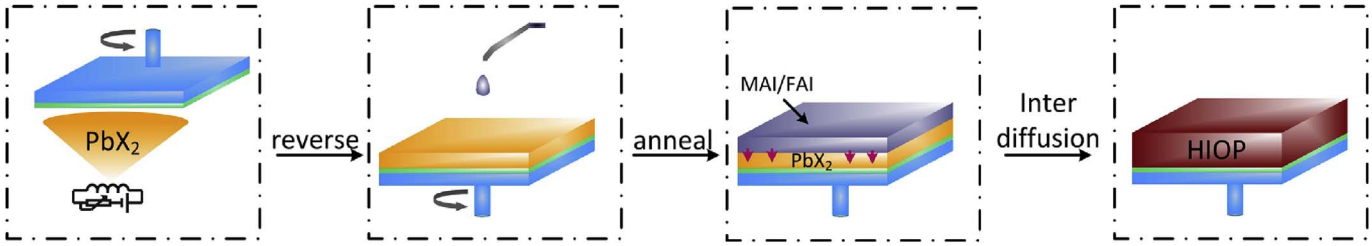

Fig. 1. Process of the vapor-solution interdiffusion protocol.

HIOP films via vapor-solution interdiffusion of vapor-deposited PbX_2 (including PbI_2, $PbBr_2$ and $PbCl_2$) and solution-deposited MAI/FAI layer. By thoroughly studying the optical properties, crystallinities, chemical components within the corresponding films and the prepared devices, potential crystal growth mechanism of the interdiffusion protocol is well explained: 1) In terms of nucleation stage, denser crystal seeds are formed in MA-HIOP than FA-HIOP due to higher nucleation rate of MA^+ ion. Particularly, using $PbCl_2$ matrix, Cl-barren phase and Cl-rich phase is first revealed for MA-HIOP and FA-HIOP, respectively. 2) As for coarsening stage, the growth rate of crystal grain in FA-HIOP surpasses that in MA-HIOP. Meanwhile, $PbCl_2$-HIOP shows greater crystal growth rate with heterogeneous phase. The best PHJ device exhibits an efficiency of 16.01% with $FAPbI_3$. We believe that this work would be a guiding light of the interdiffusion method toward further HIOPs' optoelectronic applications, such as solar cells, light-emitting diodes and lasers.

2. Experimental section

2.1. Preparation of materials

Methylammonium iodide (MAI) was synthesized via a previously reported method, in which 10 ml hydriodic acid (57 wt% in water, Sigma Aldrich) and 24 ml methylamine solution (33 wt% in ethanol, Sigma Aldrich) were stirred into 100 ml of ethanol at 0 °C for 2 h. The precipitate of MAI was obtained by a rotary evaporator. Formamidinium iodide (FAI) was synthesized using a previously reported method. 25.2 g and 48 ml of formamidinium acetate and hyriodic acid were mixed into 250 ml of methanol reacted for 2 h at room temperature. The FAI precipitate was collected by a rotary evaporator. The synthesized MAI and FAI were dried in a vacuum oven overnight. PbI_2, $PbBr_2$, $PbCl_2$ (99.999 wt%) were purchased from Alfa. PEDOT:PSS (CLEVIOS PH 1000) solution was from Haraeus and $PC_{61}BM$ (99.5%) were acquired from Haraeus and Solenne, respectively.

2.2. Fabrication of solar cells

ITO glasses were sonicated in neutral detergent and solution of acetone and ethanol for 20 min and the cleaned glasses were treated with ultraviolet ozone plasma for 5 min. PEDOT:PSS solutions were spin-coated at 1000 rpm for 30 s on cleaned ITO glasses and ITO glasses were heated at 120 °C for 20 min PbI_2, $PbBr_2$, $PbCl_2$ films of 120 nm were sublimated under a pressure of 10^{-5} mbar at a rate of 1.0 Å s^{-1} and the ITO/PEDOT:PSS/PbX_2 substrates were placed into a N_2 –filled glovebox at room temperature. MAI and FAI solutions (0.4 mol MAI/FAI in 1 ml of isopropanol (IPA)) were respectively spin-coated at 2000 rpm for 30s on substrates and were driven to interdiffusion at 80 °C for 2 h. Afterwards, the residual MAI/FAI upon the as-formed HIOP films were cleaned by spinning IPA for 2000 rpm for 30 s. Eventually, the devices were completed by consecutively vacuum deposited $PC_{61}BM$ (30 nm), BCP (6 nm) and Ag cathode (120 nm) under 10^{-5} mbar.

2.3. Characterization

The absorption spectra were acquired on a UV–vis spectrophotometer (Fluoromax 4, HORIBA Jobin Yvon, USA). The morphology was investigated by a scanning electron microscopy (SEM) (Quanta 250, FEI). The elemental composition in the corresponding films was measured by Energy Dispersive X-Ray (EDX) Spectroscopy with Standardless Quantification Model. The crystalline structures were performed by a X-ray diffraction (XRD) (D/MAX-2400, Rigaku, Japan) with Cu Kα radiation.

Device characteristics were evaluated in ambient under a AAA solar simulator (XES-301S, SAN-EI Electric. Co. Ltd.), AM 1.5G illumination with an intensity of 100 mW/cm^2. The current density-voltage (*J-V*) curves were measured by a Keithley digital source meter (Model 2602). For the inverted PHJ devices, the scan rates of current-voltage curves were performed by 0.05 V/s starting from −0.1 V to 1.2 V. The Incident Photon-to-current Conversion Efficiency (IPCE) spectra were obtained by the solar cell quantum efficiency measurement system (SolarCellScan 100, Zolix instruments. Co. Ltd). The area of each device, calibrated by the shadow mask, was 9.00 mm^2.

3. Results and discussion

The interdiffusion process of different HIOP films in our work is presented in Fig. 1. In brief, different PbX_2 films with 120 nm were initially deposited by evaporation on ITO/PEDOT:PSS (the abbreviation of poly(3,4-ethylenedioxythiophene) polystyrene sulfonate, a common hole transporting polymer) substrates in a vacuum chamber, which were sequentially transferred into a N_2-filled glovebox. Afterwards, MAI/FAI solutions dissolved in 2-propanol were respectively dripped upon the substrates and then spin-coated to cover the beneath PbX_2 film. Finally, the bilayer films were annealed to form various polycrystalline HIOP films.

We first paid attention to the morphologies as well as the crystallinities of these HIOP films by applying scanning electron microscopy (SEM) (Fig. 2a). The low magnification SEM images are also shown in Fig. S1. Systematically studying the SEM images and the corresponding crystal size distributions (Fig. 2b), we could draw some conclusions as follows: 1) To begin with, diverse crystal morphologies were achieved between different vapor-deposited PbX_2 films, mainly originating from the different bond lengths of Pb-X. Nevertheless, planar and uniform polycrystalline PbX_2 films with negligible defects and voids were readily deposited upon the substrates, which prevailed over the orthodox solution-deposited films. Naturally, the high quality films would provide a superior basic frame for as-forming HIOP films. 2) After completely thermal interdiffusion of PbX_2-MAI/FAI bilayers, the virgin PbX_2 crystals were dramatically enlarged to convert into the final HIOP crystals. More importantly, δ-phase (a non-perovskite lattice) was suppressed for $FAPbI_3$ without high thermo-energy assistance (generally > 160 °C in general 1-step method when preparing $FAPbI_3$). Compared with the coarse morphologies with scattered crystals in conventional 2-step deposition, smooth and continuous HIOP films driven by interdiffusion protocol were composed of massive closely packing crystals, which would be favourable for photo-excited carriers'

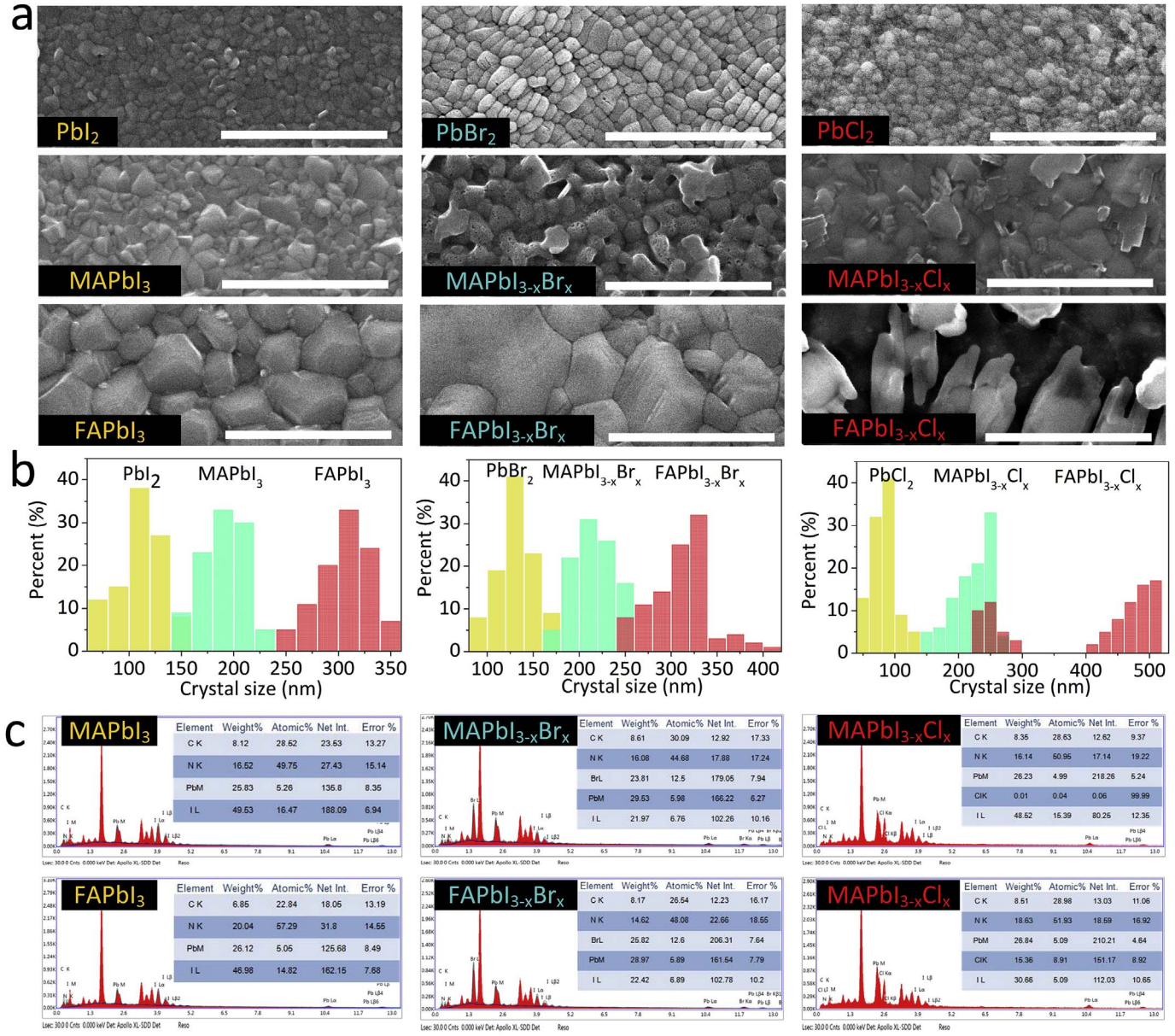

Fig. 2. (a) SEM images (scale bar: 1 μm), (b) crystal size distributions and (c) EDX results of the initial PbX_2 films and the resulting HIOP films.

diffusion. 3) The crystal sizes of HIOP films induced by FA^+ were obviously larger than the ones by MA^+, indicating the vital role of the organic cation for the crystal growth kinetics. Due to the bigger size of FA^+ (1.9 Å) than MA^+ (1.8 Å), cubic crystal lattice with slight distortion in FA-based HIOP would contribute to this crystal discrepancy. 4) HIOP films born from $PbBr_2$ showed larger crystal sizes than their colleagues from PbI_2, possibly resulting from driving original crystal lattice toward pseudocubic one by substituting I^- with small-sized Br^-. Unexpectedly, as for FA-based HIOP films from $PbCl_2$ matrix, non-hexagonal crystals lunged out of the plain, utterly differing from MA-based films. As is known, Cl could be hardly detected in the MA-based films but remained vague in FA-based ones. Thus, the odd morphology might be caused by introduction of plentiful Cl.

To address this problem, the primary element contents of the overall HIOP films were estimated by the energy dispersive X-ray (EDX) spectroscopy (Fig. 2c). Interestingly, irrespective of the organic components, the element ratio between total halogens and lead (simplified as X/Pb) was about 3.0, agreeing well with the HIOP formula $APbX_3$. Meanwhile, different halogen ratios, summarized in Table 1, revealed the halogen constitutions in these HIOP films driven by different PbX_2 frameworks. It was noted that the value of Br/I was about 2.0 for both HIOP films using $PbBr_2$, but the value of Cl/I was almost 0 and 1.75 respectively for MA-based and FA-based films using $PbCl_2$, which was consistent with the morphologies differences. Focusing on $PbCl_2$ matrix: For MA-HIOP films, most studies ascribed the negligible traces of Cl to MACl release by evaporation during thermally annealing. In contrast, the unexpected high Cl contents in FA-HIOP films here were probably caused by superior thermostability. This abnormal ratio gap of Cl/I between the two films hence interpreted the distinct crystal morphologies based on $PbCl_2$.

Table 1
Element ratio of X (halide)/I in various HIOP films from EDX.

X/I (X = I, Br, Cl)	MAI	FAI
PbI_2	1	1
$PbBr_2$	1.85	1.83
$PbCl_2$	0.002	1.75

To further evaluate the crystallographic characteristics of these

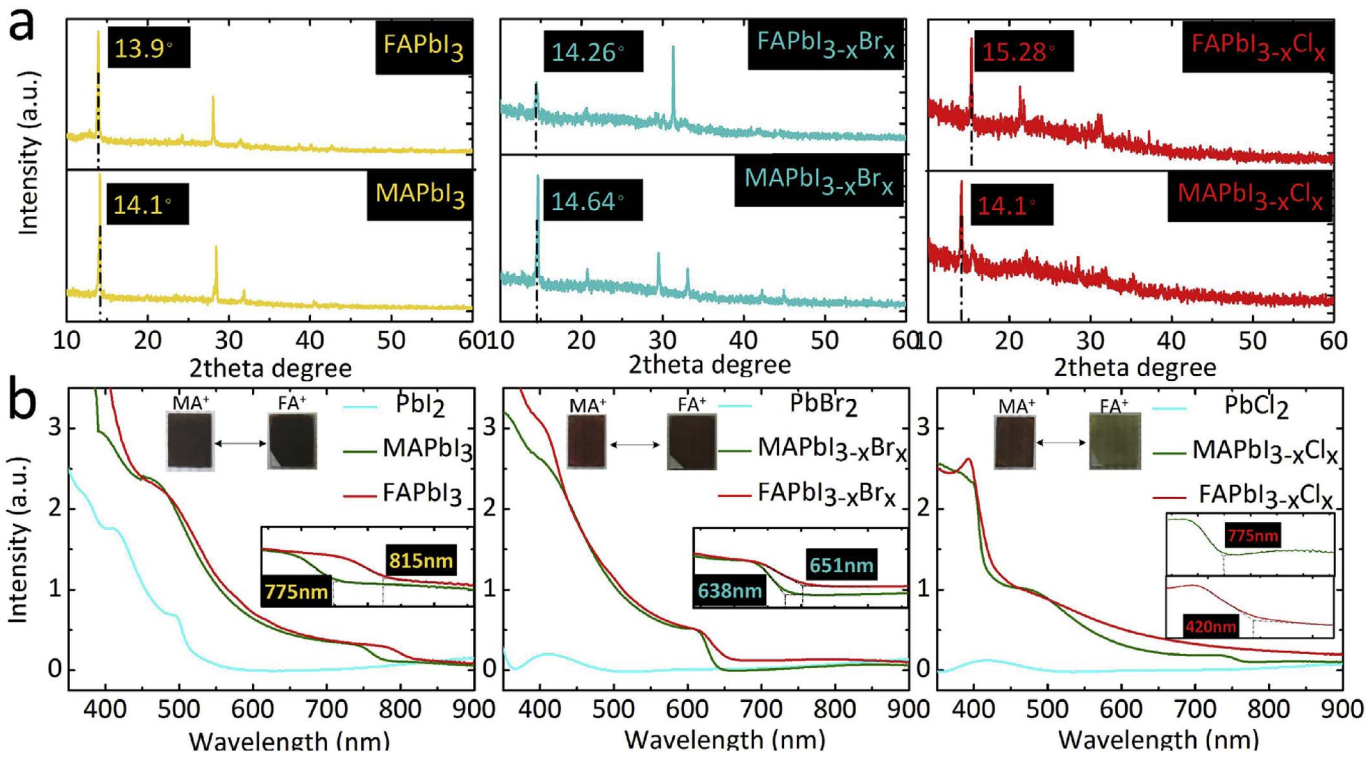

Fig. 3. (a) XRD patterns and (b) Abs spectra of various HIOP films driven by the vapor-solution interdiffusion (insets are film photographs and band edges).

HIOP films, X-ray diffraction (XRD) patterns are shown in Fig. 3a. Intriguingly, as for PbI_2 matrix, the starting predominant peak was slightly shifted from 13.9° to 14.1° when FA^+ was replaced by MA^+, indicating that tetragonal lattice ($MAPbI_3$) was formed by distortion of trigonal structure ($FAPbI_3$). Similarly, the predominant peak changing from 14.26° to 14.64° was observed for FA→MA films based on $PbBr_2$ matrix. However, it was noted that completely distinct preferential crystal growth orientation emerged for the both films, which was along (200) plane at 14.64° for MA-HIOP and (141) plane at 31.3° for FA-HIOP, similar with the prior morphology variations. For the XRD patterns of $PbCl_2$-based films, the main peak at 14.1° for MA-HIOP suggested the identical tetragonal lattice with $MAPbI_3$, which is also a signal of negligible Cl. Unfortunately, for FA-HIOP, the main diffraction peak was weirdly moved to 15.28°, revealing a Cl-rich cubic crystal phase similar to previous study [27]. Again, the altered XRD patterns confirmed conflicting crystal growth for FAI-HIOP films. Actually, we have tried to spin coat FAI for the second time or at higher concentration (0.8 mM) in $PbCl_2$ experiments. Unfortunately, unlike completely conversion into $MAPbI_3$ using MAI, the resulting HIOPs using FAI always had the similar cubic crystal patterns (shown in Fig. S2) for $FAPbCl_{1.9}I_{1.1}$ in any scenario, indicating Cl-rich phase in the final HIOP films. Accordingly, Cl-rich crystal is easily formed for FAI-HIOP when evaporated $PbCl_2$ is used as lead source.

Additionally, the photo-physical properties of these HIOP films were assessed by UV–vis absorption spectrometer (Abs). As shown in Fig. 3b, all the fabricated HIOP films exhibited much stronger absorption than their mothers' PbX_2 matrixes because of the diffusion reactions with organic ligands. Furthermore, the absorption band edges of FA-HIOP films slightly red shifted by 40 nm and 13 nm than those of MA-HIOP films for PbI_2 and $PbBr_2$ frame, suggesting that the bandgaps were reduced by 0.08 eV and 0.04 eV, respectively. Nevertheless, for $PbCl_2$, the band edge was dramatically moved from 775 nm to 420 nm as MA^+ was replaced by FA^+. This abnormal change indicated that the primitive optical bandgap (1.6 eV) was greatly broadened to 3.05 eV, a similar value as $FAPbCl_3$. Conclusively, the Abs spectra also unveiled rich Cl contents in FA-HIOP film with $PbCl_2$, which was consistent with the EDX and XRD analysis results. Except the turquoise $FAPbI_{3-x}Cl_x$ film (inside of Fig. 3b), other prepared HIOP films should be multiple choices for particular single or tandem devices. Besides, the emission peaks of steady-state PL spectra (Fig. S3) in different HIOP films agreed well with the estimated bandgaps from the corresponding Abs spectra. The enhanced PL intensity in FA-HIOP than MA-HIOP should be attributed to the suppressed nonradiative recombination with reduced crystal boundaries.

The most persuasive way to validate the interdiffusion protocol is to prepare PHJ solar cells with these versatile HIOP films. Here, all the devices adopted an inverted p-i-n planar architecture: ITO/PEDOT:PSS/HIOP/$PC_{61}BM$ ((6,6)-phenyl-C61-butyric acid methyl ester)/BCP (2,9-dimethyl-4,7-diphenyl-1,10-phenanthroline)/Ag, where $PC_{61}BM$ and BCP acted as electron transporting layer and hole blocking layer, respectively. Negligible hysteresis phenomena were found for all the *J-V* curves in Fig. S4, however, the phenomena often occurred in conventional n-i-p structures on account of significant trap defects in metal dioxide (TiO_2). Fig. 4 demonstrates the typical photocurrent density-voltage (*J-V*) curves, statistical distributions of short-circuit current density (J_{sc}) based on 20 groups of devices and the incident photon-to-current efficiency (IPCE) spectra of these devices. Based on the studies of the crystallinities and photo-physical characteristics, comprehensive device analyses could be drawn as follows: 1) Except $PbCl_2$ matrix, the J_{sc} of FA-HIOP devices were much higher than those of MA-HIOP devices, which was mainly induced by their uniform large-sized crystals. All the IPCE spectra of these HIOP devices resembled the corresponding Abs spectra, revealing higher photocurrents of FA-HIOP than MA-HIOP in Fig. 4b. Besides, the integrated J_{sc} values from IPCE spectra in Fig. S5 were close to the measured J_{sc} from *J-V* curves, which proved the reliable device performances. Accordingly, the resulting power conversion efficiencies (PCEs) would be increased by substituting MA with FA, as shown in PCE statistical distributions (Fig. S6). 2) Meanwhile, FA-HIOP devices had lower open circuit voltage (V_{oc}) due to their narrow bandgaps. 3) As for $PbBr_2$ matrix, although the distinct crystal growth direction between the two HIOP films, no evident recession of J_{sc} appeared, indicating the more importance of film quality rather than

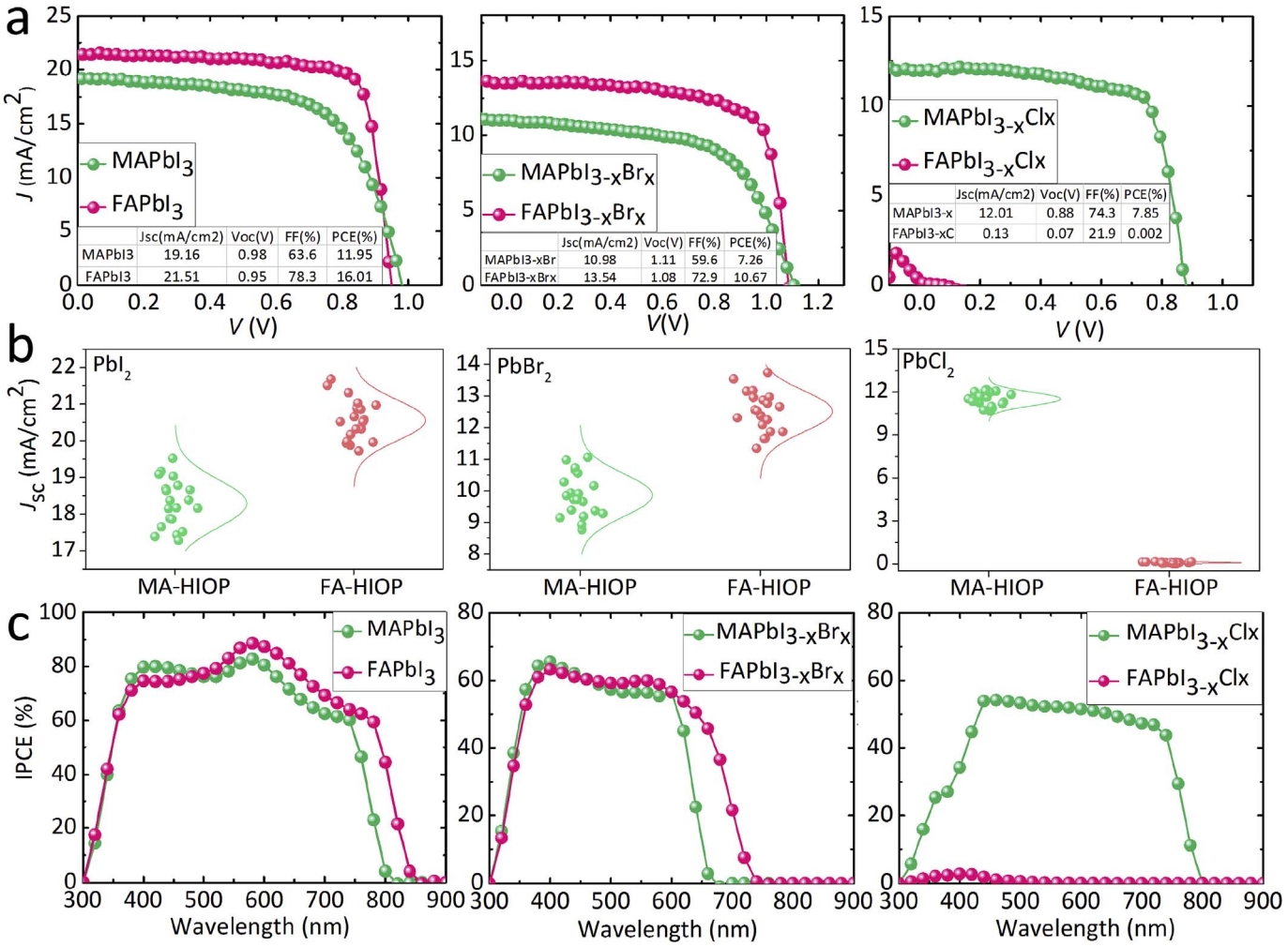

Fig. 4. (a) Typical *J-V* curves, (b) statistical distributions of J_{sc} and (c) corresponding IPCE spectra of the PHJ devices based on various HIOP films (insets of (a) are the photovoltaic parameters).

crystallinity growth orientation. 4) In terms of $PbCl_2$ matrix, only MAI-HIOP device exhibited pretty photovoltaic performance thanks to its similar properties with $MAPbI_3$ films. Actually, some reports suggested the deposition of superb $MAPbI_3$ films was more controllable with $PbCl_2$ (or MACl) auxiliary [31–33]. However, the values of J_{sc} and PCE were still uncompetitive than other films due to the lower absorption intensity. On the contrary, device using FA-HIOP became almost invalid with a J_{sc} of 0.13 mA/cm^2, a V_{oc} of 0.07 V, a FF of 21.9% and a PCE of 0.002%. We believe that not only the overlarge bandgap but also the poor film quality was detrimental for light capture and exciton dissociation. Consequently, it demonstrated that $FAPbI_3$ deposition should avoid $PbCl_2$ inclusion into precursors to introduce Cl-rich phase into the HIOP films. 5) Hysteresis index (HI) is used to evaluate the hysteresis degree between the forward sweep and reverse sweep, which is defined as [35,36]

$$HI = (PCE_{FS} - PCE_{RS}) / PCE_{RS}$$

where PCE_{FS} is the PCE in forward sweep direction, PCE_{RS} is the PCE in reverse sweep direction. We have summarized the PCEs and calculated HIs of different perovskite based devices in Table S1. It can be observed that based on PbI_2 and $PbBr_2$, the HI values of FA-based devices were obviously higher compared to MA-based devices, indicating the reduced exciton recombination rates with fewer crystal grain boundaries. But based on $PbCl_2$, the HI value of FA-based device was much higher compared to MA-based devices. These abnormal results maybe result from the poor film morphology and limited short-wavelength light absorption. Hence, FA-based perovskites can contribute to suppressed *J-V* hysteresis except for $PbCl_2$ frame.

Considering the full-scale analyses of these HIOP films fabricated by controlling the initial precursors, the essential crystal growth mechanism driven by interdiffusion protocol was presumed based on a classical theory: For the first stage, compact and uniform PbX_2 polycrystalline films by vapor were deposited on substrates and then organic salt layers were closely adhered to them. Afterwards, moderate annealing impelled the double layers to react mutually:

$$PbX_2 + MAI/FAI \rightarrow MAPbI_{3-y}X_y/FAPbI_{3-y}X_y \ (X = I, y = 0)$$

Typically, the stages of polycrystalline films formation can be divided into nucleation and coarsening. However, the two stages would be proceeding simultaneously during interdiffusion.

1) Well-proportioned crystal nuclei at the film surfaces were immediately formed as soon as the substrates were annealed owing to the homogeneity of the beneath PbX_2 layers. Then, MAI/FAI gradually diffused deeply into PbX_2 bulks with various rates determining by the thermodynamics until PbX_2 was depleted. The penetrating depth (Z) of the resulting films is described according to a previous literature [37]

$$Z^2 = Kt$$

where K is a rate constant determined by $K'\exp(-Q/RT)$ (Q is activation energy of the reaction, R is the gas constant, T is absolute temperature), t is reaction time. Because of identical t and T during the reaction, Q plays the vital role for the final HIOP films, which is chiefly depended

on halogens and organic components. As is known, the crystal lattice of HIOP is structured by inserting MAI/FAI into virgin PbX_2 frame. Actually, considering different chemical stability of each intermediate, the natural reaction process, so as to the final crystal lattice, became more complicated. In order to simplify the nucleation reaction, we envisaged two scenarios as follows (i. and ii.): i. Halogens within PbX_2 frame were hypothesized as invariable during interdiffusion. In this way, the category of the organic salts would dominate the reaction. We inferred that MA^+ with smaller size would flow faster throughout the bulk than FA^+ since PbI_2 film immediately became black once MAI solutions were dropped. The XRD patterns of these films (Fig. S7 in the manuscript) proved partial HIOP conversion for MAI but almost no change for FAI. This meant that MAI had the higher penetration depth Z compared to FAI. Due to $Z^2 = Kt$, where t was identical, we can speculate $K(\text{MAI}) > K(\text{FAI})$. ii. Organic component was constant. Chemical band (μ) between these PbX_2 was considered as μ(Pb-I) < μ(Pb-Br) < μ(Pb-Cl). For PbI_2, due to no other "polluting" halogens (Br or Cl) and weak bond in the interdiffusion system, single $MAPbI_3$ or $FAPbI_3$ phase was ensured even partial I position in PbI_2 was replaced with excess I in MAI/FAI. The process could be explained by:

$$PbI_2 + (y+1)MAI \rightarrow MAPbI_3 + yMAI(g)\uparrow$$

$$PbI_2 + (y+1)FAI \rightarrow FAPbI_3 + yFAI(g)\uparrow$$

For $PbBr_2$, it could be speculated the HIOP formula was $MAPbIBr_2$/$FAPbIBr_2$ from the ratio of Br/I was around 2.0 by EDX, indicating Br within $PbBr_2$ was not easily substituted by I (maybe due to stronger chemical bond of Pb-Br). In this similar way, this reaction was drawn as:

$$PbBr_2 + (y+1)MAI \rightarrow MAPbIBr_2 + yMAI(g)\uparrow$$

$$PbBr_2 + (y+1)FAI \rightarrow MAPbIBr_2 + yFAI(g)\uparrow$$

For $PbCl_2$, the reaction system seemed more complex with various organic salts. When MAI was applied, the final HIOP showed a crystal structure like $MAPbI_3$ with negligible Cl, uncovering that overall Cl within original $PbCl_2$ was almost exhausted by I in the MAI diffusion period, despite the strongest chemical bond of Pb-Cl. Zhang et al. pointed out that intermediate product MACl was very easy to be volatilized on account of its lower decomposition temperature than MAI [17]. Moreover, Yin et al. used a first-principle calculation to indicate the overlarge formation energy of I/Cl alloy MA-HIOP than I/Br or Br/Cl analogues [38]. Consequently, the possible diffusion reaction could be interpreted by:

$$PbCl_2 + 3MAI \rightarrow MAPbI_3 + 2MACl(g)\uparrow$$

However, when FAI was used to react with $PbCl_2$, the atom ratio of Cl/I in the final HIOP was about 1.75, unraveling a formed Cl-rich cubic lattice with widened bandgap. Unlike the scenario of MA, large-sized stable FAI with lower diffusion kinetics possibly needed extra thermo-energy to form $FAPbI_3$, rather than $FAPbCl_3$. In other words, the weak formation energy of $FAPbCl_3$ potentially suppressed $FAPbI_3$ formation. Accordingly, the distinct reaction of $FAPbCl_{1.9}I_{1.1}$ (formulated with EDX result) was surmised as:

$$PbCl_2 + (y+1.1)FAI \rightarrow FAPbCl_{1.9}I_{1.1} + 0.1FACl(g)\uparrow + yFAI(g)\uparrow$$

Above all, we summarized the nucleation reaction process as illustrated in Fig. 5.

2) In the meanwhile, the formed nuclei started to grow and coarsen over time. The hexagonal crystal grains began to grow horizontally by consuming neighbour grains with fewer sides [39,40]. Referring to the high crystallinities of FAI-HIOP films than MAI-HIOP films, we deduced that large-sized FA^+ would rapidly induce more regular cubic lattice with less distortion, so as to the final grains with increased radius. As for $PbBr_2$ matrix, I (in MAI/FAI) as heterogeneous nuclei would boost the hybrid HIOP crystals coarsened than pure $XPbI_3$. The crystal grain evolution of $PbCl_2$ matrix with MAI showed a similar tendency with $PbBr_2$-HIOP. However, the growth with FAI almost went out of control because of the imbalanced kinetics between $FAPbI_3$ and $FAPbCl_3$.

The most important kinetics parameter is the crystal coarsening rate constant in the coarsening stage, which determines the final crystal size. According to the previous reported [37]

$$r^2\text{-}r_0{}^2 = K_2t$$

where r_0 and r is the crystal size at time zero and at time t, K_2 is the coarsening rate constant. Because the perovskites were converted from PbX_2 in the beginning, we set the average crystal size of PbX_2 as r_0. We have summarized corresponding r_0 and r (Table 2) of different perovskite films from Fig. 2b. Considering that the coarsening time t was 7200 s (or 2 h), the coarsening rate constant K_2 can be obtained in Table 2 by calculation. From the value of K_2 in the summary data, we can draw the conclusion that

$$K_2 \text{ (FA-HIOP)} > K_2 \text{ (MA-HIOP)}$$

$$K_2 \text{ (PbCl}_2\text{-HIOP)} > K_2 \text{ (PbBr}_2\text{-HIOP)} > K_2 \text{ (PbBr}_2\text{-HIOP)}$$

Finally, grains coarsening evolution of the corresponding HIOP film was also shown in Fig. 5.

For HIOP crystal growth kinetics comparison between evaporated and solution process, we have prepared lead iodide film with solution process by spin-coating DMF and DMSO solutions (1 mM). The morphologies and crystal size distributions of the corresponding PbI_2 films and prepared perovskite films are shown in Fig. S8. Using the coarsening kinetics equation $r^2\text{-}r_0{}^2 = K_2t$, we can estimate that the value of K_2 ($*10^{-14}$ cm^2/s) for the corresponding perovskite based on evaporation, DMF and DMSO driven PbI_2 film was 3.78, 3.63 and 30.33, respectively. We found that PbI_2 film from evaporation and DMF had almost same coarsening rate constant for the final perovskites. However, PbI_2 film from DMSO showed the highest coarsening rate constant, which should be ascribed to DMSO molecules coordination within PbI_2 film to slow down the perovskite crystal formation.

4. Conclusion

In summary, the underlying interdiffusion mechanism was elucidated by thoroughly analyzing the polycrystalline HIOP films with subtly tuning each component of the precursors. The potential crystal growth process of various HIOPs could be considered as following: 1) Nucleation stage: the faster nucleation rate of MA-HIOP always led to denser crystal seeds and uncontrolled morphologies than FA-HIOP. Particularly, when $PbCl_2$ was used as lead source, Cl-barren phase for MA-HIOP and Cl-rich phase for FA-HIOP were recognized for conflicting crystal structure. 2) Coarsening stage: the crystal growth kinetics of the as-formed FA-HIOP films and $PbCl_2$-films suppressed that of other HIOP films on account of adequate crystal nuclei space and heterogeneous phase assistance. The corresponding performances of our fabricated PHJ solar cells also agreed with the validated mechanism, showing a champion efficiency of 16.01% with $FAPbI_3$. Substantially, this work will instruct us to realize different target HIOP ($MAPbI_{3-x}Br_x$, $MAPbI_{3-x}Cl_x$ or $FAPbI_{3-x}Br_x$) films toward versatile photovoltaic devices by interdiffusion protocol (or other solution methods) with selective precursors (such as PbX_2, organic components).

Acknowledgment

This work was financially supported by National Natural Science Foundation of China (Grant No. 11574248), International Cooperation by Shaanxi (Grant No. 2015KW-008), China Postdoctoral Science Foundation (Grant No. 2016M590947) and the Fundamental Research Funds for the Central Universities (Grant No. xjj2016031). The SEM work was implemented at International Centre for Dielectric Research (ICDR), Xi'an Jiaotong University, Xi'an, China. The authors also thank

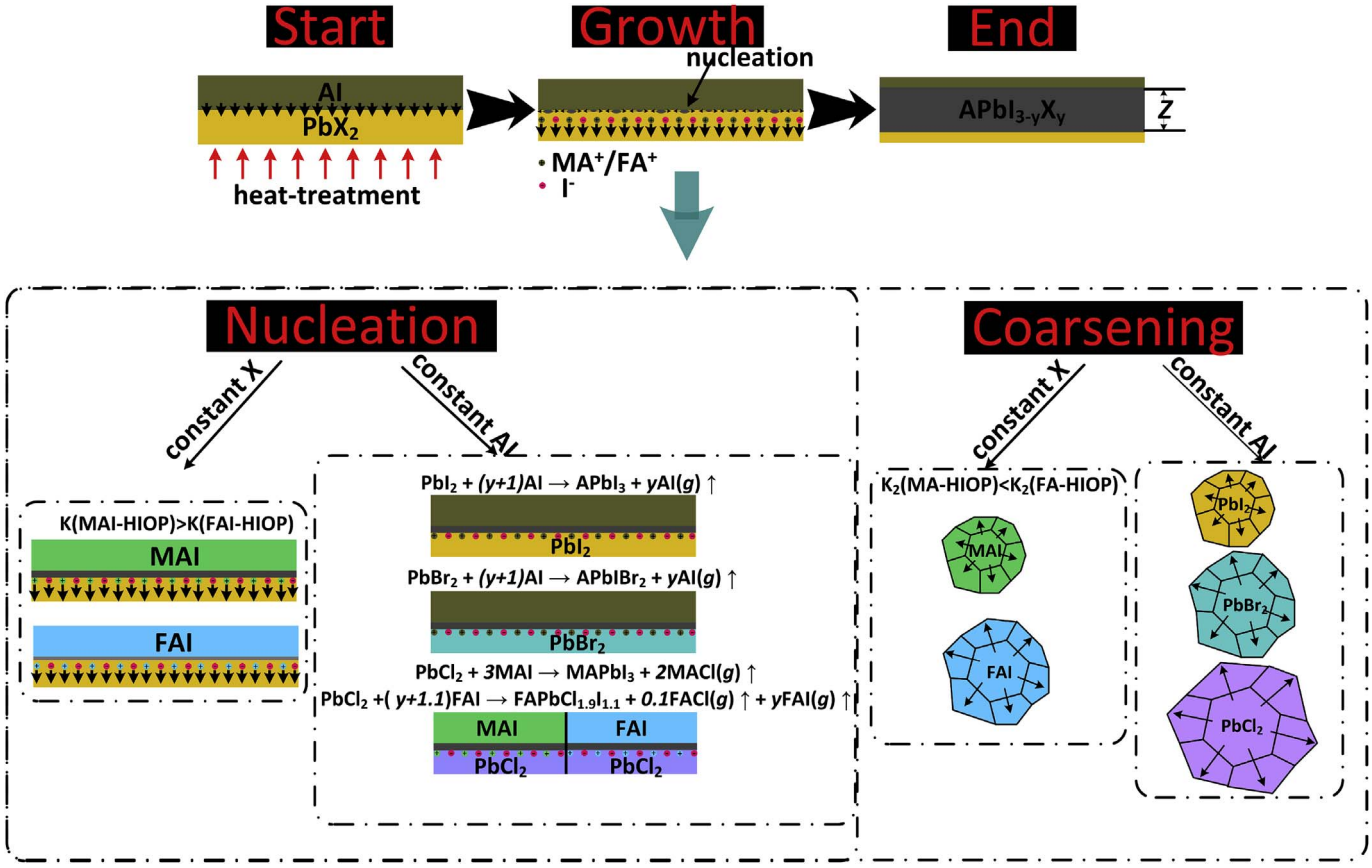

Fig. 5. The schematic illustration of the HIOP nucleation and coarsening stages in the solution-interdiffusion system.

Table 2
Corresponding r_0, r and coarsening rate constant K_2 of different perovskite films.

HIOP material		r_0 (nm)	r (nm)	K_2 (*10^{-14} cm^2/s)
PbI_2	MAI	110.8	189.8	3.78
	FAI		298.2	10.64
$PbBr_2$	MAI	125.2	215.2	4.26
	FAI		318.6	11.92
$PbCl_2$	MAI	82.2	221.8	5.89
	FAI		362.4	17.3

Mr. Ma for his help in using SEM.

Appendix A. Supplementary data

Supplementary data related to this article can be found at http://dx.doi.org/10.1016/j.orgel.2017.11.011.

References

[1] A. Kojima, K. Teshima, Y. Shirai, T. Miyasaka, J. Am. Chem. Soc. 131 (2009) 6050–6051.
[2] W.S. Yang, J.H. Noh, N.J. Jeon, Y.C. Kim, S. Ryu, J. Seo, S.I. Seok, Science 348 (2015) 1234–1237.
[3] National Renewable Energy Laboratory, Best research-cell efficiencies chart, http://www.nrel.gov/ncpv/images/efficiency_chart.jpg.
[4] T. Leijtens, J. Lim, J. Teuscher, T. Park, H.J. Snaith, Adv. Mater 25 (2013) 3227–3233.
[5] S.D. Stranks, G.E. Eperon, G. Grancini, C. Menelaou, M.J.P. Alcocer, T. Leijtens, L.M. Herz, A. Petrozza, H.J. Snaith, Science 342 (2013) 341–343.
[6] C. Wehrenfennig, G.E. Eperon, M.B. Johnston, H.J. Snaith, L.M. Herz, Adv. Mater 26 (2014) 1584.
[7] G. Xing, N. Mathews, S. Sun, S.S. Lim, Y.M. Lam, M. Grätzel, S. Mhaisalkar, T.C. Sum, Science 342 (2013) 344–347.
[8] J. Xi, Z. Wu, B. Jiao, H. Dong, C. Ran, C. Piao, T. Lei, T.-Z. Song, W. Ke, T. Tokoyama, X. Hou, M.G. Kanatzidis, Adv. Mater 29 (2017) 1606964.
[9] C. Ran, Z. Wu, J. Xi, F. Yuan, H. Dong, T. Lei, X. He, X. Hou, J. Phys. Chem. Lett. 8 (2017) 394–400.
[10] N.G. Jeon, J.H. Noh, Y.C. Kim, W.S. Yang, S. Ryu, S.I. Seok, Nat. Mater 13 (2014) 897–903.
[11] J.-H. Im, I.-H. Jang, N. Pellet, M. Grätzel, N.-G. Park, Nat. Nanotech 9 (2014) 927–932.
[12] P.-W. Liang, C.-Y. Liao, C.-C. Chueh, F. Zuo, S.T. Williams, X.-K. Xin, J. Lin, A.K.-J. Jen, Adv. Mater 26 (2014) 3748–3754.
[13] M. Xiao, F. Huang, W. Huang, Y. Dkhissi, Y. Zhu, J. Etheridge, A. Gary-Weale, U. Bach, Y.-B. Cheng, L. Spiccia, Angew. Chem. Int. Ed. 53 (2014) 9898–9903.
[14] Z. Xiao, C. Bi, Y. Shao, Q. Dong, Q. Wang, Y. Yuan, C. Wang, Y. Gao, J. Huang, Energy Environ. Sci. 7 (2014) 2619–2623.
[15] Z. Xiao, Q. Dong, C. Bi, Y. Shao, Y. Yuan, J. Huang, Adv. Mater 26 (2014) 6503–6509.
[16] W. Nie, H. Hsai, R. Asadpour, J.-C. Blancon, A.J. Neukirch, G. Gupta, J.J. Crochet, M. Chhowalla, S. Tretiak, M.A. Alam, H.-L. Wang, A.D. Mohite, Science 347 (2015) 522–525.
[17] W. Zhang, S. Pathak, N. Sakai, T. Stergiopoulos, P.K. Nayak, N.K. Noel, A.A. Haghighirad, V.M. Burlakov, D.W. deQuilettes, A. Sadhanala, W. Li, L. Wang, D.S. Ginger, R.H. Friend, H.J. Snaith, Nat. Commun. 6 (2015) 10030.
[18] H. Liu, Z. Huang, S. Wei, L. Zheng, L. Xiao, Q. Gong, Nanoscale 8 (2016) 6209–6221.
[19] D. Zheng, G. Yang, Y. Zheng, P. Fan, R. Ji, J. Huang, W. Zhang, J. Yu, Electrochim. Acta 247 (2017) 548–557.
[20] Q. Hu, J. Wu, C. Jiang, T. Liu, X. Que, R. Zhu, Q. Gong, ACS Nano 8 (2014) 10161–10167.
[21] J. Xi, Z. Wu, H. Dong, B. Xia, F. Yuan, B. Jiao, L. Xiao, Q. Gong, X. Hou, Nanoscale 7 (2015) 10699–10707.
[22] F. Fu, T. Feurer, T. Jäger, E. Avancini, B. Bissig, S. Yoon, S. Buecheler, A.N. Tiwari, Nat. Commun. 6 (2015) 8932.
[23] J. Xi, Z. Wu, K. Xi, H. Dong, B. Xia, T. Lei, F. Yuan, W. Wu, B. Jiao, X. Hou, Nano Energy 26 (2016) 438–445.
[24] J.H. Noh, S.H. Im, J.H. Heo, T.N. Mandal, S.I. Seok, Nano Lett. 13 (2013) 1764–1769.
[25] Y. Zhao, K. Zhu, J. Am. Chem. Soc. 136 (2014) 12241–12244.
[26] C. Bi, Y. Yuan, Y. Fang, J. Huang, Adv. Energy Mater 5 (2015) 1401616.
[27] A. Sadhanala, S. Ahmad, B. Zhao, N. Giesbrecht, P.M. Pearce, F. Deschler, R.L.Z. Hoye, K.C.G. del, T. Bein, P. Docampo, S.E. Dutton, M.F.L. De Volder, R.H. Friend, Nano Lett. 15 (2015) 6095–6101.
[28] G.E. Eperon, S.D. Stranks, C. Menelaou, M.B. Johnston, L.M. Herz, H.J. Snaith, Energy Environ. Sci. 7 (2014) 982–988.
[29] N.J. Jeon, J.H. Noh, W.S. Yang, Y.C. Kim, S. Ryu, J. Seo, S.I. Seok, Nature 517

(2015) 476–480.
[30] J. Liu, Y. Shirai, X. Yang, Y. Yue, W. Chen, Y. Wu, A. Islam, L. Han, Adv. Mater 27 (2015) 4918–4923.
[31] S.T. Williams, F. Zuo, C.-C. Chueh, C.-Y. Liao, P.-W. Liang, A.K.Y. Jen, ACS Nano 8 (2014) 10640–10654.
[32] Q. Chen, H. Zhou, Y. Fang, A.Z. Stieg, T.-B. Song, H.-H. Wang, X. Xu, Y. Liu, S. Lu, J. You, P. Sun, J. McKay, M.S. Goorsky, Y. Yang, Nat. Commun. 6 (2015) 7269.
[33] H. Yu, F. Wang, F. Xie, W. Li, J. Chen, N. Zhao, Adv. Funct. Mater 24 (2014) 7102–7108.
[34] Y. Li, W. Sun, W. Yan, S. Ye, H. Peng, Z. Liu, Z. Bian, C. Huang, Adv. Funct. Mater 25 (2015) 4867–4873.
[35] R.S. Sanchez, V. Gonzalez-Pedro, J.-W. Lee, N.-G. Park, Y.S. Kang, I. Mora-Sero, J. Bisquert, J. Phys. Chem. Lett. 5 (2014) 2357–2363.
[36] H.-S. Kim, N.-G. Park, J. Phys. Chem. Lett. 5 (2014) 2927–2934.
[37] Y. Zhou, O.S. Game, S. Pang, N.P. Padture, J. Phys. Chem. Lett. 6 (2015) 4827–4839.
[38] W.-J. Yin, Y. Yan, S.-H. Wei, J. Phys. Chem. Lett. 5 (2014) 3625–3631.
[39] J. Schlipf, P. Docampo, C.J. Schaffer, V. Krstgens, L. Bießmann, F. Hanusch, N. Giesbrecht, S. Bernstorff, T. Bein, P. Müller-Buschbaum, J. Phys. Chem. Lett. 6 (2015) 1265–1269.
[40] B. Yang, J. Keum, O.S. Ovchinnikova, A. Belianinov, S. Chen, M.-H. Du, I.N. Ivanov, C.M. Rouleau, D.B. Geohegan, K. Xiao, J. Am. Chem. Soc. 138 (2016) 5028–5035.